

Cite this: *Nanoscale Adv.*, 2020, 2, 2018

# A magnetic $\gamma\text{-Fe}_2\text{O}_3\text{@PANI@TiO}_2$ core–shell nanocomposite for arsenic removal *via* a coupled visible-light-induced photocatalytic oxidation–adsorption process†

Yuan Wang,<sup>a</sup> Ping Zhang,<sup>a</sup> Tian C. Zhang,<sup>b</sup> Gang Xiang,<sup>c</sup> Xinlong Wang,<sup>a</sup> Simo Pehkonen<sup>d</sup> and Shaojun Yuan<sup>ib</sup>\*<sup>a</sup>

Arsenic polluted groundwater impairs human health and poses severe threats to drinking water supplies and ecosystems. Hence, an efficient method of simultaneous oxidation of As(III) to As(V), and removal of As(V) from water has triggered increasing attention. In this study, a magnetic  $\gamma\text{-Fe}_2\text{O}_3$  core–shell heterojunction nanocomposite was synthesized by means of hydrothermal crystallization of  $\text{TiO}_2$  on the surface of the magnetic core–shell loaded with polyaniline ( $\gamma\text{-Fe}_2\text{O}_3\text{@PANI@TiO}_2$ ). As an efficient photocatalyst coupled with adsorption,  $\gamma\text{-Fe}_2\text{O}_3\text{@PANI@TiO}_2$  has a high light utilization and good adsorption capacity. Notably, the nanocomposite has excellent stability at various initial pH values with good reusability. Among the co-existing ions investigated,  $\text{PO}_4^{3-}$  has the greatest competitive reaction. The photocatalytic oxidation of As(III) on  $\gamma\text{-Fe}_2\text{O}_3\text{@PANI@TiO}_2$  is dominated by the synergy of several active substances, with superoxide free radicals and photogenerated holes being the major players.

Received 29th February 2020  
Accepted 30th March 2020

DOI: 10.1039/d0na00171f

rsc.li/nanoscale-advances

## Introduction

Arsenic is one of the many metal elements in the water environment, soil, rocks as well as in the atmosphere, and poses a serious threat due to its strong toxicity to humans and other species.<sup>1–3</sup> The transformation and migration of arsenic to the biota come mainly from the water environment. Since groundwater is a main source of drinking water in many countries, its safe level in water is of vital importance to human life and ecology in general.<sup>4,5</sup> Mexico, Bangladesh, India, Vietnam, China, Argentina, Chile and other 22 different countries or regions in the world are affected by arsenic pollution.<sup>6–8</sup> Particularly, in Bangladesh 40 million people are reported to be at risk of arsenic poisoning.<sup>9</sup> Therefore, it is imperative to develop advanced treatment systems to remove aquatic arsenic.

The common arsenic species in groundwater include As(III) (arsenite) and As(V) (arsenate), and its specific form is affected by the redox potential (ORP) and pH.<sup>10,11</sup> As(III) has greater

toxicity and mobility than As(V), leading to the poor performance of many of the removal technologies of As(III).<sup>12</sup> An efficient approach is to oxidize As(III) to As(V) *via* a pre-treatment process as As(V) can be easily removed through adsorption, ion exchange, and coagulation.<sup>13</sup> Recently, photocatalytic degradation methods have received considerable attention.<sup>14–16</sup> Among them, the UV/ $\text{TiO}_2$  system distinguishes itself by its stability and low cost.<sup>17–21</sup> However,  $\text{TiO}_2$  delivers only a limited adsorption capacity, resulting in an inefficient removal capacity.<sup>22,23</sup> Therefore, development of systems for efficient oxidation of As(III) to As(V) and simultaneous removal of As(V) has received increasing attention.

Yoon *et al.* used activated alumina to achieve photocatalytic oxidation and adsorption of As(III) in both Fenton and UV/ $\text{TiO}_2$  systems. After four hours of reaction, the total arsenic removal efficiency could reach 90%.<sup>23</sup> Miller *et al.* applied  $\text{TiO}_2$  impregnated chitosan beads to arsenic removal; these beads exhibited a sorption capacity of  $6.4 \text{ mg g}^{-1}$  for As(III) under UV light but only  $2.2 \text{ mg g}^{-1}$  without UV light.<sup>24</sup> Although photocatalytic oxidation coupled with adsorption for arsenic removal has triggered increasing attention, this technology still has several weaknesses, such as low light utilization efficiency, low quantum efficiency, and poor adsorption capacity. Solving the above problems relies mainly on expanding the light absorption wavelength range, increasing the light absorption rate and thereby enhancing catalyst's visible light reactivity. Thus, the current knowledge gap is how to enhance the activity and

<sup>a</sup>Low-carbon Technology & Chemical Reaction Engineering Lab, College of Chemical Engineering, Sichuan University, Chengdu 610065, China. E-mail: ysj@scu.edu.cn

<sup>b</sup>Civil and Environmental Engineering Department, University of Nebraska-Lincoln, Omaha, NE 68182-0178, USA

<sup>c</sup>College of Physical Science and Technology, Sichuan University, Chengdu 610064, China

<sup>d</sup>Department of Environmental and Biosciences, University of Eastern Finland, 70211 Kuopio, Finland

† Electronic supplementary information (ESI) available. See DOI: 10.1039/d0na00171f



efficiency of the photocatalyst for arsenic removal by modifying the structure and composition of the catalyst.

As a conductive polymer, polyaniline (PANI) is inherently a good electron donor and a carrier of photogenerated holes.<sup>25,26</sup> Meanwhile, PANI can promote the carrier migration rate, restrain the electron-hole recombination, and expand the light absorption to the visible region and improve the quantum efficiency of light utilization.<sup>27–29</sup> In addition, previous studies showed that maghemite ( $\gamma\text{-Fe}_2\text{O}_3$ ) has excellent adsorption properties in wastewater treatment.<sup>30–32</sup>  $\gamma\text{-Fe}_2\text{O}_3$  can efficiently adsorb As(v) onto the surface, and then be easily separated under a magnetic field.<sup>33,34</sup> Therefore, we hypothesize that  $\text{TiO}_2$  on the surface of the  $\gamma\text{-Fe}_2\text{O}_3$  core-shell loaded with PANI ( $\gamma\text{-Fe}_2\text{O}_3\text{@PANI@TiO}_2$ ) would significantly enhance the photocatalytic adsorption of As(III).

In this work, for the first time we have synthesized/optimized  $\gamma\text{-Fe}_2\text{O}_3\text{@PANI@TiO}_2$ , a bifunctional material for highly efficient removal of As(III). This letter reports several aspects of our investigation, including the performance of the new material under the influence of initial pH, co-existing ions, initial As(III) concentrations and the dosage of the catalyst; the removal kinetics; the reusability and the associated mechanism of the photocatalytic oxidation of As(III).

## Experimental

### Materials and methods

**Synthesis of  $\gamma\text{-Fe}_2\text{O}_3$ .** All chemicals were of analytical grade and used as received without further purification. 10.81 g of  $\text{FeCl}_3 \cdot 6\text{H}_2\text{O}$  was dissolved in 40 mL of deionized water; then a 250 mL solution containing 6 g of NaOH was added to the  $\text{FeCl}_3$  solution under mechanical stirring, and heated to boil for 10 minutes before natural cooling; then 250 mL of 0.01 M  $\text{HNO}_3$  solution was used to mix the component solutions; then the precursor was collected and washed with deionized water by centrifugation until the solution pH was 7. 11.93 g of  $\text{FeCl}_2 \cdot 4\text{H}_2\text{O}$  was dissolved in 20 mL of deionized water; then 4.2 g of NaOH was dissolved in 250 mL of deionized water. The precursor was then added to the  $\text{FeCl}_2$  solution, and the NaOH solution was added under mechanical stirring; then the solution was heated using an electric heating sleeve until boiling, and was kept for 30 minutes before natural cooling, and a precipitate was obtained. Then 0.01 M  $\text{HNO}_3$  solution was mixed with the precipitate and centrifuged until the washing solution was neutral. Finally, the cleaned product was vacuum-dried at 50 °C for 48 h, and the product was  $\text{Fe}_3\text{O}_4$ .  $\gamma\text{-Fe}_2\text{O}_3$  was obtained after  $\text{Fe}_3\text{O}_4$  was annealed at 300 °C for 2 h in an air atmosphere (Fig. 1).

**Synthesis of  $\gamma\text{-Fe}_2\text{O}_3\text{@PANI}$ .** 0.4 g of  $\gamma\text{-Fe}_2\text{O}_3$  was added to 80 mL of 0.5 M  $\text{H}_2\text{SO}_4$  solution in an ice bath. Then, 1 g of aniline monomer was added to the above solution with mechanical stirring. Then, 4.56 g of ammonium persulfate as the initiator was added to the above solution, which then was kept in an ice bath for 6 h. Finally, the product was vacuum-dried at 50 °C for 48 h. Pure PANI was prepared under the same conditions.



Fig. 1 Schematic illustration of the preparation procedure of  $\gamma\text{-Fe}_2\text{O}_3\text{@PANI@TiO}_2$ .

**Synthesis of  $\gamma\text{-Fe}_2\text{O}_3\text{@PANI@TiO}_2$ .** After drying, a mass of 0.2 g of  $\gamma\text{-Fe}_2\text{O}_3\text{@PANI}$  was weighed and dissolved in 120 mL of deionized water. After 30 minutes of ultrasonic water bath mixing, the  $\gamma\text{-Fe}_2\text{O}_3\text{@PANI}$  was dispersed evenly. Then, 0.8 g of  $\text{TiO}_2$  (P25, provided by Chengdu Kelong Chemical Reagent Co., Ltd) was added to the above solution slowly and mechanically stirred for 30 minutes at 100 RPM to dissolve and fully disperse the  $\text{TiO}_2$ . Then, the solution was transferred to a 150 mL PPL-lined high pressure reaction vessel, which was sealed and placed in an electric drum air desiccant box, and the hydrothermal crystallization reaction was conducted at 120 °C for 24 h. After the reaction, a large amount of deionized water and anhydrous ethanol were used repeatedly and the product was centrifuged to remove unreacted  $\text{TiO}_2$  and other impurities. Finally, the product was freeze-dried at –50 °C for 24 h, and the obtained product is known as the  $\gamma\text{-Fe}_2\text{O}_3\text{@PANI@TiO}_2$  heterojunction composite material.

**Characterization and experiments.** The characterization and experiments are shown in the ESI.†

## Results and discussion

Fig. S1† shows the visual appearance comparison of  $\gamma\text{-Fe}_2\text{O}_3\text{@PANI@TiO}_2$ ,  $\gamma\text{-Fe}_2\text{O}_3\text{@PANI}$ , and  $\gamma\text{-Fe}_2\text{O}_3$ . The Fourier transform infrared (FTIR) spectra are shown in Fig. 2a. The two bands at  $3443\text{ cm}^{-1}$  and  $1638\text{ cm}^{-1}$  are attributed to the –OH stretching vibration of surface water and the –OH bending vibration absorption of surface water molecules or carboxyl groups, respectively. The band at  $675\text{ cm}^{-1}$  for  $\text{TiO}_2$  corresponds to the Ti–O–Ti stretching vibration.<sup>35</sup> For  $\gamma\text{-Fe}_2\text{O}_3$ , the peak at  $1383\text{ cm}^{-1}$  corresponds to the characteristic peak of O–H deformation, and the absorption within the range of  $500\text{--}800\text{ cm}^{-1}$  is attributed to the Fe–O stretching vibration.<sup>36</sup> After PANI coating, the spectrum of  $\gamma\text{-Fe}_2\text{O}_3\text{@PANI}$  shows the characteristic peaks of  $\gamma\text{-Fe}_2\text{O}_3$  and PANI.<sup>37,38</sup> When  $\text{TiO}_2$  was introduced onto the  $\gamma\text{-Fe}_2\text{O}_3\text{@PANI}$ , a new absorption peak at  $1057\text{ cm}^{-1}$  appeared, corresponding to the C–O–Ti stretching.<sup>39</sup> It is clear that the formation of  $\text{Fe}_2\text{O}_3\text{@PANI@TiO}_2$  is successful. Due to the high content of  $\text{TiO}_2$ , the characteristic peaks of





Fig. 2 Characterization of  $\text{TiO}_2$ ,  $\gamma\text{-Fe}_2\text{O}_3$ ,  $\gamma\text{-Fe}_2\text{O}_3\text{@PANI}$ , and  $\gamma\text{-Fe}_2\text{O}_3\text{@PANI@TiO}_2$ : (a) FTIR spectra, (b) Raman spectra, (c) XRD spectra, and (d) thermogravimetric analysis (TG) curves.

the nanocomposite and  $\text{TiO}_2$  are relatively consistent, while the peaks of other components are mostly suppressed. In Fig. 2b, the absorption of  $E_g$ ,  $B_{1g}$  and  $A_{1g}$  Raman activity characteristics of  $\text{TiO}_2$  at 142, 199, 394, 516, and  $638\text{ cm}^{-1}$  is observed.<sup>40</sup> After introducing  $\text{TiO}_2$  onto the  $\gamma\text{-Fe}_2\text{O}_3\text{@PANI}$ , the  $\gamma\text{-Fe}_2\text{O}_3\text{@PANI@TiO}_2$  mainly displays the characteristic peak of  $\text{TiO}_2$  with a weak peak of PANI, indicating the relatively high loading of  $\text{TiO}_2$ .

The X-ray diffraction (XRD) pattern of  $\gamma\text{-Fe}_2\text{O}_3\text{@PANI}$  exhibits the (220), (311), (400), (422), (511), and (440) planes of  $\gamma\text{-Fe}_2\text{O}_3$ ,<sup>41</sup> and a weak broad peak in the range of  $15\text{--}25^\circ$  deriving from the characteristic of PANI, which indicates the successful synthesis of  $\gamma\text{-Fe}_2\text{O}_3\text{@PANI}$  (Fig. 2c). After loading  $\text{TiO}_2$  onto the  $\gamma\text{-Fe}_2\text{O}_3\text{@PANI}$ , all peaks of  $\gamma\text{-Fe}_2\text{O}_3\text{@PANI@TiO}_2$  correspond to the nature of  $\text{TiO}_2$  and  $\gamma\text{-Fe}_2\text{O}_3$ . The characteristic peak of PANI cannot be observed, indicating the high loading of  $\text{TiO}_2$ , which is consistent with the result of Raman spectra. As shown in Fig. 2d,  $\gamma\text{-Fe}_2\text{O}_3$  has less weight loss, indicating the good thermal stability. For  $\gamma\text{-Fe}_2\text{O}_3\text{@PANI}$ , the decomposition temperature in the range of  $180\text{--}600^\circ\text{C}$  mainly corresponds to the weight loss of the PANI oligomer, doping agent, and the branched polymer chain. A rapid weight loss is observed at a temperature of  $730^\circ\text{C}$ , which is due to the decomposition of the outer structure of PANI. In the range of  $730\text{--}850^\circ\text{C}$ , the rate of weight loss is 10%, indicating the pyrolyzation of benzene and quinone ring structures. Notably,  $\text{Fe}_2\text{O}_3\text{@PANI@TiO}_2$  exhibits a good thermal stability, which is due to the introduction of  $\text{TiO}_2$  onto  $\gamma\text{-Fe}_2\text{O}_3\text{@PANI}$ .

The composite material prepared by the hydrothermal crystallization has a good dispersion (Fig. 3a). The high magnification transmission electron microscopy (TEM) image (Fig. 3b) shows a few lattice planes with a  $d$ -spacing of  $0.352\text{ nm}$ , corresponding to the (101) plane of  $\text{TiO}_2$ , and of  $0.295\text{ nm}$  corresponding to the (220) plane of  $\gamma\text{-Fe}_2\text{O}_3$ . The blurry section between  $\text{TiO}_2$  and  $\gamma\text{-Fe}_2\text{O}_3$  could be attributed to the amorphous

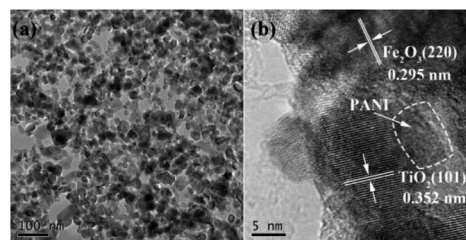


Fig. 3 TEM images of the surface morphology of  $\gamma\text{-Fe}_2\text{O}_3\text{@PANI@TiO}_2$  nanocomposites at (a) low magnification and (b) high magnification.

PANI. Fig. S2† shows the scanning electron microscopy (SEM) images of  $\gamma\text{-Fe}_2\text{O}_3\text{@PANI@TiO}_2$ . In addition, the morphologies of  $\gamma\text{-Fe}_2\text{O}_3$  and  $\gamma\text{-Fe}_2\text{O}_3\text{@PANI}$  were also studied by TEM technology. Fig. S3† shows the low magnification TEM images of  $\gamma\text{-Fe}_2\text{O}_3$ , indicating the morphology of nanoparticles with the size in the range of  $10\text{--}50\text{ nm}$ . Fig. S4† shows the  $\gamma\text{-Fe}_2\text{O}_3$  surrounded by amorphous PANI, which corresponds to the result in Fig. 3b. All results strongly support the successful synthesis of  $\gamma\text{-Fe}_2\text{O}_3\text{@PANI}$ .

Fig. S5a† exhibits the  $\text{N}_2$  adsorption–desorption isotherms of  $\gamma\text{-Fe}_2\text{O}_3$ ,  $\gamma\text{-Fe}_2\text{O}_3\text{@PANI}$ , and  $\gamma\text{-Fe}_2\text{O}_3\text{@PANI@TiO}_2$  at  $77\text{ K}$ . According to the IUPAC classification, all samples show the characteristics of type IV isotherms with an H3 hysteresis loop. No saturated adsorption platform occurs when the value of  $p/p_0$  is high, indicating an irregular pore structure. Fig. S5b† shows that the three samples have a similar nature, mainly distributed at  $30\text{--}70\text{ nm}$ , and concentrated in the mesopore range. PANI coating has a small effect on the pore volume, while an increased pore volume is obtained after introducing  $\text{TiO}_2$ . Table S1† clearly shows that  $\gamma\text{-Fe}_2\text{O}_3\text{@PANI@TiO}_2$  exhibits a high specific surface area, which could provide more active sites for the adsorption of  $\text{As}(\text{III})$ .

The wide spectrum obtained from X-ray photoelectron spectroscopy (XPS) (Fig. 4a) exhibits that the binding energies (BEs) of C 1s, N 1s, Ti 2p, O 1s, and Fe 2p are  $284.3$ ,  $400.0$ ,  $458.7$ ,  $529.9$ , and  $710.6\text{ eV}$ , respectively. The N 1s XPS spectrum (Fig. 4b) shows that amine ( $-\text{NH}-$ ) with BEs at  $400.0\text{ eV}$  occupies prominent character in nitrogen atoms.<sup>42</sup> Imines ( $=\text{N}-$ ) and



Fig. 4 (a) XPS spectrum of  $\gamma\text{-Fe}_2\text{O}_3\text{@PANI@TiO}_2$ . XPS spectra of (b) N 1s, (c) Ti 2p, (d) Fe 2p, (e) C 1s and (f) O 1s regions.



positively charged nitrogen ( $N^+$ ) are also observed. The Ti 2p spectrum (Fig. 4c) exhibits two peaks with BEs at 458.3 and 463.9 eV, corresponding to Ti 2p<sub>3/2</sub> and Ti 2p<sub>1/2</sub>, respectively.<sup>43</sup> The Fe 2p XPS spectrum (Fig. 4d) shows two peaks at 710.9 and 724.9 eV that are ascribed to Fe 2p<sub>3/2</sub> and Fe 2p<sub>1/2</sub>.<sup>41,44,45</sup> The C 1s spectrum shown in Fig. 4e can be deconvoluted into four components with BEs at about 284.3, 285.1, 286.0 and 288.5 eV, corresponding to C–H, C–N, C–O, and O=C–O, respectively. The O 1s spectrum (Fig. 4f) can be deconvoluted into three peaks; the BEs at 532.9, 531.5, and 529.7 eV can be ascribed to H<sub>2</sub>O (H–O–H), hydroxide (O–H), and oxide (Fe–O and Ti–O), respectively.<sup>42,43</sup> The XPS patterns show the successful formation of the heterojunction, in good agreement with the results of XRD and FTIR.

Fig. S6 and Table S2† show the magnetization curves and detailed comparison of  $\gamma$ -Fe<sub>2</sub>O<sub>3</sub>@PANI@TiO<sub>2</sub>,  $\gamma$ -Fe<sub>2</sub>O<sub>3</sub>@PANI, and  $\gamma$ -Fe<sub>2</sub>O<sub>3</sub>. A magnetic nuclear shielding effect can be observed after introduction of PANI (43.20 emu g<sup>-1</sup>) and TiO<sub>2</sub> (18.51 emu g<sup>-1</sup>), while the magnitude of coercive force was not significantly affected, remaining at around 120 Oe. Fig. S7a† shows the UV-vis DRS spectra of all samples. It is noted that the absorption increased from 400 nm for TiO<sub>2</sub> to 500 nm for  $\gamma$ -Fe<sub>2</sub>O<sub>3</sub>@PANI@TiO<sub>2</sub>, which implies that the absorption of such a heterogeneous junction composite is in the visible light region. Fig. S7b† clearly shows that the  $\gamma$ -Fe<sub>2</sub>O<sub>3</sub>@PANI@TiO<sub>2</sub> exhibits a narrower forbidden bandwidth (2.49 eV) than TiO<sub>2</sub> (3.16 eV), indicating transition of more photoelectrons in such a heterogeneous junction composite.

Arsenic removal experiments by photocatalytic oxidation and adsorption are carried out under visible light derived from a Xe lamp with a luminous intensity of 500 W. In the process of photocatalytic oxidation of arsenic, the solution pH will affect the species distribution of arsenic, the surface characteristics of the catalyst, and the position of the energy band, thus affecting the transformation and surface adsorption of As(III)/As(V). Fig. 5a shows that the total arsenic removal onto the composite material is basically stable (7–9 mg g<sup>-1</sup>) within an initial pH

range of 2–10, which is a limitation for using some adsorbents.<sup>46,47</sup> Based on the pH range of typical arsenic-containing groundwater, a pH of 5.0 was selected to be the initial solution pH in later experiments. Fig. 5b indicates that TiO<sub>2</sub>, PANI, and  $\gamma$ -Fe<sub>2</sub>O<sub>3</sub> deliver only a low capacity for arsenic removal, but  $\gamma$ -Fe<sub>2</sub>O<sub>3</sub>@PANI@TiO<sub>2</sub> has an outstanding capacity, implying that such a heterogeneous junction composite is superior to TiO<sub>2</sub> and  $\gamma$ -Fe<sub>2</sub>O<sub>3</sub> for arsenic removal.

Fig. 5c shows that As removal increases but gradually levels off with an increase in the initial concentration of As(III), presumably due to the limitation of active sites. Fig. 5d shows that Cl<sup>-</sup>, Ca<sup>2+</sup>, and Mg<sup>2+</sup> have almost no negative effect on the As adsorption capacity, while NO<sub>3</sub><sup>-</sup> and CO<sub>3</sub><sup>2-</sup> have a weak inhibitory effect. However, the corresponding removal capacity of As decreased by 17% in the presence of SO<sub>4</sub><sup>2-</sup> and 45% in the presence of PO<sub>4</sub><sup>3-</sup>, indicating that SO<sub>4</sub><sup>2-</sup> and PO<sub>4</sub><sup>3-</sup> are greatly competitive. Stability is critical to the catalyst for the photocatalytic oxidation of As. Fig. 5e shows that in the initial and fifth cycles the extent of photocatalytic oxidation of As(III) can reach 75% and 55%, respectively. Fig. 5f exhibits the As removal capacity of  $\gamma$ -Fe<sub>2</sub>O<sub>3</sub>@PANI@TiO<sub>2</sub> in successive tests; it still delivers a removal capacity of 6.83 mg g<sup>-1</sup> and a retention rate of 77.8% after 5 cycling tests. The decreased catalytic activity could be ascribed to the increased recombination of electron-hole pairs, thus reducing the charge separation efficiency. This is further confirmed by photoluminescence measurement (Fig. S8†), which shows that  $\gamma$ -Fe<sub>2</sub>O<sub>3</sub>@PANI@TiO<sub>2</sub> delivers a more significant fluorescence signal in the visible spectrum after the recycling test.

The kinetics of dark adsorption and light reaction were also investigated. The surface adsorption kinetics and fitting curves of  $\gamma$ -Fe<sub>2</sub>O<sub>3</sub>@PANI@TiO<sub>2</sub> are shown in Fig. 6a. Within 30 minutes in the dark, the adsorption of As(III) on  $\gamma$ -Fe<sub>2</sub>O<sub>3</sub>@PANI@TiO<sub>2</sub> reached up to 90% of the total adsorption quantity, and the rate became slow after 60 minutes with the active hydroxy and amino adsorption sites on the surface being

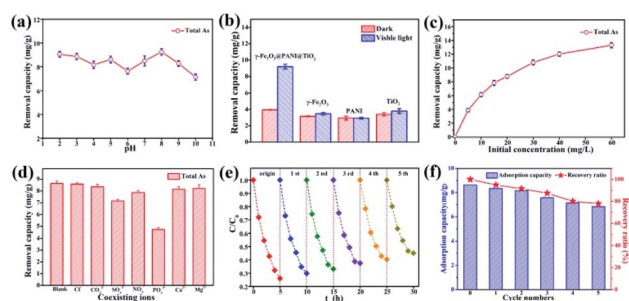


Fig. 5 (a) The arsenic removal capacity of  $\gamma$ -Fe<sub>2</sub>O<sub>3</sub>@PANI@TiO<sub>2</sub> in solutions with various initial pH. (b) The arsenic removal capacity with different adsorbents in the dark and under visible light. (c) The arsenic removal capacity of  $\gamma$ -Fe<sub>2</sub>O<sub>3</sub>@PANI@TiO<sub>2</sub> at various initial concentrations of As(III). (d) The effect of co-existing ions on arsenic removal by the  $\gamma$ -Fe<sub>2</sub>O<sub>3</sub>@PANI@TiO<sub>2</sub>. (e) Recycling experiment of the photocatalytic oxidation activity of the  $\gamma$ -Fe<sub>2</sub>O<sub>3</sub>@PANI@TiO<sub>2</sub> toward As(III). (f) Recycling experiments of the total As removal by the  $\gamma$ -Fe<sub>2</sub>O<sub>3</sub>@PANI@TiO<sub>2</sub>.

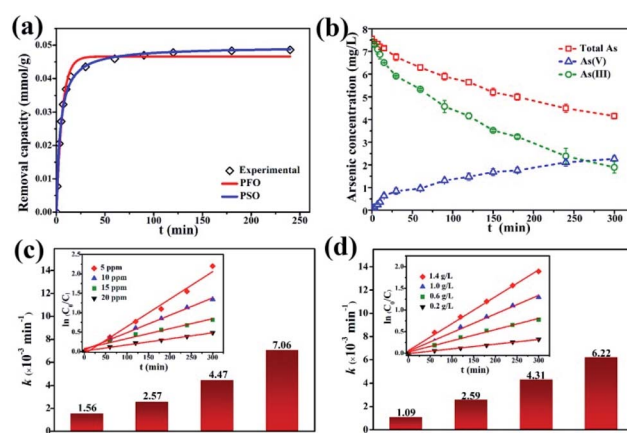


Fig. 6 Kinetics analysis of  $\gamma$ -Fe<sub>2</sub>O<sub>3</sub>@PANI@TiO<sub>2</sub>: (a) adsorption kinetics in the dark, (b) reaction kinetics of As(III) and As(V) under a Xe lamp, (c) the reaction rate constants and fitting curves (inset) at various initial As(III) concentrations, and (d) the reaction rate constants and fitting curves (inset) at various concentrations of the catalyst.



occupied. By fitting the adsorption data with the pseudo-first-order (PFO) and pseudo-second-order (PSO) kinetics model<sup>46,48</sup> (Table S3†), the PSO model was found to be better with the corresponding non-linear fitting coefficient of Chi-square ( $\chi^2$ ) being as low as  $0.970 \times 10^{-6}$  and the corresponding  $R^2$  being 0.996. Therefore, the adsorption process of As(III) onto  $\gamma$ -Fe<sub>2</sub>O<sub>3</sub>@PANI@TiO<sub>2</sub> is classified as chemical adsorption. Fig. 6b shows the reaction kinetics of all the arsenic species, including total arsenic, As(III), and As(V). After dark adsorption, the total arsenic concentration in the solution is 7.5 mg L<sup>-1</sup>. It is noted that As(V) keeps accumulating in the solution and its concentration continually increases, while the total arsenic concentration decreases gradually. After 300 min of light irradiation, the concentration of As(V) in the solution is higher than that of As(III), accounting for 54% of the total arsenic. The adsorption process of As(III) is almost balanced, and its photocatalytic oxidation efficiency reaches 75%. The results suggest that the  $\gamma$ -Fe<sub>2</sub>O<sub>3</sub>@PANI@TiO<sub>2</sub> heterojunction composite is effective for removal of aqueous As(III) by a coupled photocatalytic oxidation/adsorption process.

The initial concentration of As(III) is critical to photocatalytic oxidation. The kinetics curves and fitting results of the photocatalytic oxidation of As(III) at different initial As(III) concentrations are shown in Fig. S9a† and Fig. 6c. It can be seen that as the initial As(III) concentration increases, the reaction rate constant decreases. The higher the As(III) concentration is, the more As(III) is likely to adsorb onto the catalyst; however, As(III) itself may also absorb photons, thereby reducing the utilization of light energy by  $\gamma$ -Fe<sub>2</sub>O<sub>3</sub>@PANI@TiO<sub>2</sub>, and thus causing the reaction rate constant to decrease. At the initial As(III) and catalyst concentration of 5 mg L<sup>-1</sup> and 1 g L<sup>-1</sup>, the efficiency of As(III) removal can reach 89%. In addition, Fig. S9b† and Fig. 6d show that  $\gamma$ -Fe<sub>2</sub>O<sub>3</sub>@PANI@TiO<sub>2</sub> for As(III) photo-oxidation follows the PFO reaction law of the photocatalytic oxidation process, which is in agreement with earlier reports.<sup>49,50</sup> Therefore, the reaction process is not only related to the photocatalytic oxidation process, but also affected by adsorption.

To further investigate the possible photocatalytic oxidation mechanism, silver nitrate (AgNO<sub>3</sub>), ammonium oxalate (AO), benzoquinone (BQ), and isopropanol (IPA) were selected as the trapping reagents for electrons, light generated surface holes, superoxide free radicals, and hydroxyl free radicals, respectively.<sup>12</sup> As(III) oxidation extent was measured in the presence or absence (blank) of the four reagents. Fig. 7a shows the dynamics curve comparison of photocatalytic oxidation of As(III) in the presence of the different trapping agents. Almost no oxidation of As(III) is observed for the case without adding any catalyst. AgNO<sub>3</sub> and IPA have a weak inhibitory effect on the oxidation of As(III), indicating that both electrons and hydroxyl radicals have a small effect on the transformation of As(III) to As(V). With AO as the trapping reagent, the As(III) oxidation rate is only 36% ( $C/C_0 = 64\%$ ) after 5 h of illumination, confirming that photo-produced holes play an important role in the photocatalytic reaction process. For the reaction system with BQ added, the  $C/C_0$  was as high as 80%, indicating that the effect of superoxide free radicals was the most prevalent during the As(III) photocatalytic oxidation. Fig. S10† shows the fitting curves and the

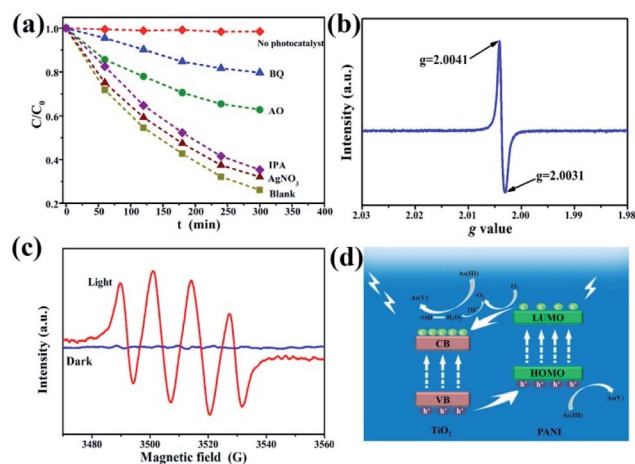


Fig. 7 (a) Kinetics of As(III) photocatalytic oxidation in the presence of different free radical trapping reagents. ESR spectra of the  $\gamma$ -Fe<sub>2</sub>O<sub>3</sub>@PANI@TiO<sub>2</sub> for (b) light generated holes and (c) DMPO-<sup>-</sup>O<sub>2</sub>. (d) Schematic illustration of the postulated mechanism of As(III) photocatalytic oxidation on the  $\gamma$ -Fe<sub>2</sub>O<sub>3</sub>@PANI@TiO<sub>2</sub>.

corresponding reaction rate constants. Therefore, the four kinds of active substances for the As(III) photocatalytic oxidation are operative and in the following order: superoxide free radicals > light generated surface holes  $\gg$  hydroxyl radicals and electrons. In this process, however, the oxidation of As(III) is due to several active substances and their interactions, instead of a single active oxidizer.

In order to further identify the existence of photogenerated holes and superoxide free radicals, electron spin resonance (ESR) technology was used. The ESR spectrum of photo-generated holes (Fig. 7b) shows that the  $g$  values of the composites are 2.0031 and 2.0041, respectively, and the center of symmetry is 2.0036, corresponding to the Ti<sup>4+</sup>-trapped hole.<sup>51</sup> Generally the  $g$  value of TiO<sub>2</sub> is in the range of 2.0–2.03, and Fe<sup>3+</sup> can occupy the site of formation of dissolved oxygen free radicals, which affects the  $g$  value displacement with doped substances to 2.004. Fig. 7c shows the ESR spectra of oxygen-containing free radicals under the conditions of dark and visible light. 5,5-Dimethyl-1-pyrroline *N*-oxide (DMPO) was used as the spin-trapping agent. In the dark, no signal is observed, because TiO<sub>2</sub> does not have sufficient potential to convert O<sub>2</sub> to <sup>-</sup>O<sub>2</sub>. However, four response signals related to the DMPO-<sup>-</sup>O<sub>2</sub> are obtained under light irradiation (Fig. 7c).<sup>52</sup> These results indicate that under visible light irradiation  $\gamma$ -Fe<sub>2</sub>O<sub>3</sub>@PANI@TiO<sub>2</sub> can produce photoreactive holes and superoxide (hydroperoxy) free radicals, both of which would act as active species in the photocatalytic oxidation of As(III).

On the basis of the experimental results and other previous studies,<sup>53–55</sup> we propose the mechanism of photocatalytic oxidation of As(III) in the visible light system (Fig. 7d). Under visible light irradiation, the low energy level of TiO<sub>2</sub> with electrons (*i.e.*, VB) absorbs light energy, and the photogenerated holes can transfer to PANI's highest occupied orbital (HOMO) (higher than the valence band of TiO<sub>2</sub>). The lowest empty orbital (LUMO) of PANI is higher than the conduction band of TiO<sub>2</sub>. Therefore,



electrons transfer to the TiO<sub>2</sub> conduction band, which prompts the electrons and holes to move in an opposite direction in the composite catalytic material, reducing the undesirable hole-electron recombination rate, and creating more photogenerated holes. In addition, under weakly acidic conditions, oxygen free radicals ( $^{\cdot}\text{O}_2^-$ ) and  $\text{H}^+$  can react to generate hydrogen peroxide. The decomposition of unstable hydrogen peroxide continues, thereby generating hydroxide ions, oxygen, and hydroxyl radicals.<sup>56</sup> Hydroxyl radicals can also participate in the As(III) oxidation process although with smaller effects (Fig. 7a). During the oxidation of As(III) to As(V), hydroperoxy free radicals, photo-generated holes, and hydroxyl free radicals play a synergistic role, with the first two being dominant.

## Conclusions

In summary,  $\gamma\text{-Fe}_2\text{O}_3@\text{PANI}@\text{TiO}_2$  has been demonstrated as an effective photocatalytic oxidation adsorbent for As(III) removal. Compared to its precursors TiO<sub>2</sub> and  $\gamma\text{-Fe}_2\text{O}_3$ , such a bifunctional material delivers a superior As(III) removal efficiency under visible light. Notably, it also shows excellent stability at various initial pH values. The investigation of co-existing ions shows that  $\text{PO}_4^{3-}$  has the greatest competitive reaction. The photocatalytic oxidation kinetics of As(III) coincides with the first-order reaction law, which is governed by a coupled photocatalytic oxidation and adsorption. The initial concentration of the catalyst and As(III) can significantly affect the kinetics of the photocatalytic oxidation; a higher concentration of the catalyst and a lower concentration of As(III) correspond to a higher rate constant. The photocatalytic oxidation of As(III) on the magnetic  $\gamma\text{-Fe}_2\text{O}_3@\text{PANI}@\text{TiO}_2$  heterojunction nanocomposite is dominated by the synergy of several active substances with superoxide free radicals and photogenerated holes being the major players. This work provides a new catalyst for As(III) removal and the associated mechanism of the photocatalytic oxidation of As(III) is clearly elucidated, which may open up an exciting new window for the rational design and application of heterojunction nanocomposites for photocatalytic oxidation.

## Conflicts of interest

There are no conflicts to declare.

## Acknowledgements

The authors are grateful for the financial support of the National Natural Science Foundation of China (21676169, 21978182), the measurement of XRD and Raman spectra by the Institute of New Energy and Low Carbon Technology of Sichuan University, and XPS measurement by Ceshigo Research Service (<http://www.ceshigo.com>).

## References

- 1 Y. Kim, K. Choi, J. Jung, S. Park, P. Kim and J. Park, *Environ. Int.*, 2007, **33**, 370–375.
- 2 M. Gonzalez-Pleiter, S. Gonzalo, I. Rodea-Paomares, F. Leganes, R. Rosal, K. Boltes, E. Marco and F. Fernandez-Pinas, *Water Res.*, 2013, **47**, 2050–2064.
- 3 M. Amini, K. C. Abbaspour, M. Berg, L. Winkel, S. J. Hug, E. Hoehn, H. Yang and C. A. Johnson, *Environ. Sci. Technol.*, 2008, **42**, 3669–3675.
- 4 Q. Li, N. J. Eate and J. K. Shang, *Environ. Sci. Technol.*, 2009, **43**, 1534–1539.
- 5 X. Luo, C. Wang, S. Luo, R. Dong, X. Tu and G. Zeng, *Chem. Eng. J.*, 2012, **187**, 45–52.
- 6 H. Guo, D. Stuben and Z. Berner, *J. Colloid Interface Sci.*, 2007, **315**, 47–53.
- 7 D. Vu, X. Li and C. Wang, *Sci. China: Chem.*, 2012, **56**, 678–684.
- 8 V. K. Gupta, V. K. Saini and N. Jain, *J. Colloid Interface Sci.*, 2005, **288**, 55–60.
- 9 M. Piri, M. Martikainen, K. Ainassaari, T. Kuokkanen and R. L. Keiski, *J. Colloid Interface Sci.*, 2011, **353**, 257–262.
- 10 P. L. Smedley and D. G. Kinniburgh, *Appl. Geochem.*, 2002, **17**, 517–568.
- 11 S. Wang and C. N. Mulligan, *Sci. Total Environ.*, 2006, **366**, 701–721.
- 12 J. Zhu, Z. Zhu, H. Zhang, H. Lu, W. Zhang, Y. Qiu, L. Zhu and S. Kuppers, *Appl. Catal., B*, 2018, **225**, 550–562.
- 13 US EPA, *Technologies and costs for removal of arsenic from drinking water*, Washington, DC, 2000.
- 14 P. Kar, P. Jain, V. Kumar and R. K. Gupta, *J. Environ. Chem. Eng.*, 2019, **7**, 102843.
- 15 P. Jain, A. Kumar, N. Verma and R. K. Gupta, *Sol. Energy*, 2019, **189**, 35–44.
- 16 B. Balasubramaniam, N. Singh, P. Kar, A. Tyagi, J. Prakash and R. K. Gupta, *Mol. Syst. Des. Eng.*, 2019, **4**, 804–827.
- 17 N. Singh, R. Chakraborty and R. K. Gupta, *J. Environ. Chem. Eng.*, 2018, **6**, 459–467.
- 18 N. Singh, J. Prakash, M. Misra, A. Sharma and R. K. Gupta, *ACS Appl. Mater. Interfaces*, 2017, **9**, 28495–28507.
- 19 M. Misra, N. Singh and R. K. Gupta, *Catal. Sci. Technol.*, 2017, **7**, 570–580.
- 20 N. Singh, K. Mondal, M. Misra, A. Sharma and R. K. Gupta, *RSC Adv.*, 2016, **6**, 48109–48119.
- 21 M. Misra, R. K. Gupta, A. K. Paul and M. Singla, *J. Power Sources*, 2015, **294**, 580–587.
- 22 W. Zhou, H. G. Fu, K. Pan, C. G. Tian, Y. Qu, P. P. Lu and C. C. Sun, *J. Phys. Chem.*, 2008, **112**, 19584–19589.
- 23 S. Yoon and J. H. Lee, *J. Ind. Eng. Chem.*, 2007, **13**, 97–104.
- 24 S. M. Miller and J. B. Zimmerman, *Water Res.*, 2010, **44**, 5722–5729.
- 25 W. Cui, J. He, H. Wang, J. Hu, L. Liu and Y. Liang, *Appl. Catal., B*, 2018, **232**, 232–245.
- 26 X. C. Wang, K. Maeda, A. Thomas, K. Takanabe, G. Xin, J. M. Carlsson, K. Domen and M. Antonietti, *Nat. Mater.*, 2009, **8**, 76.
- 27 L. Jing, Z. Yang, Y. Zhao, Y. Zhang, X. Guo, Y. Yan and K. Sun, *J. Mater. Chem. A*, 2014, **2**, 1068–1075.
- 28 L. Liu, L. Ding, Y. Liu, W. An, S. Lin, Y. Liang and W. Cui, *Appl. Catal., B*, 2017, **201**, 92–104.



- 29 L. Ge, C. Han and J. Liu, *J. Mater. Chem. A*, 2012, **22**, 11843–11850.
- 30 T. Tuutijärvi, J. Lu, M. Sillanpää and G. Chen, *J. Hazard. Mater.*, 2009, **166**, 1415–1420.
- 31 J. Yang, H. Zhang, M. Yu, I. Emmanuelawati, J. Zou, Z. Yuan and C. Yu, *Adv. Funct. Mater.*, 2014, **24**, 1354–1363.
- 32 F. Mou, J. Guan, H. Ma, L. Xu and W. Shi, *ACS Appl. Mater. Interfaces*, 2012, **4**, 3987–3993.
- 33 Z. Wu, W. Li, P. A. Webley and D. Zhao, *Adv. Mater.*, 2012, **24**, 485–491.
- 34 F. Mou, J. Guan, Z. Xiao, Z. Sun, W. Shi and X. Fan, *J. Mater. Chem.*, 2011, **21**, 5414–5421.
- 35 P. M. Kumar, S. Badrinarayanan and M. Sastry, *Thin Solid Films*, 2000, **358**, 122–130.
- 36 X. Wang, L. Gao, H. Zheng, M. Ji, T. Shen and Z. Zhang, *J. Cryst. Growth*, 2004, **269**, 489–492.
- 37 G. Sun, B. Dong, M. Cao, B. Wei and C. Hu, *Chem. Mater.*, 2011, **23**, 1587–1593.
- 38 H. H. dos Santos, C. A. Demarchi, C. A. Rodrigues, J. M. Greneche, N. Nedelko and A. Slawska-Waniewska, *Chemosphere*, 2011, **82**, 278–283.
- 39 Y. Lin, D. Li, J. Hu, G. Xiao, J. Wang, W. Li and X. Fu, *J. Phys. Chem. C*, 2012, **116**, 5764–5772.
- 40 X. Zeng, X. Sun, Y. Yu, H. Wang and Y. Wang, *Chem. Eng. J.*, 2019, **378**, 122226.
- 41 C. Jia, L. Sun, F. Luo, X. Han, L. J. Heyderman, Z. Yan, C. Yan, K. Zheng, Z. Zhang, M. Takano, N. Hayashi, M. Eltschka, M. Kläui, U. Rüdiger, T. Kasama, L. Cervera-Gontard, R. E. Dunin-Borkowski, G. Tzvetkov and J. Raabe, *J. Am. Chem. Soc.*, 2008, **130**, 16968–16977.
- 42 X. Lu, X. Chen, W. Zhou, Y. Tong and G. Li, *ACS Appl. Mater. Interfaces*, 2015, **7**, 14843–14850.
- 43 Y. Wang, K. Jia, Q. Pan, Y. Xu, Q. Liu, G. Cui, X. Guo and X. Sun, *ACS Sustainable Chem. Eng.*, 2019, **7**, 117–122.
- 44 K. Li, X. Liu, T. Zheng, D. Jiang, Z. Zhou, C. Liu, X. Zhang, Y. Zhang and D. Losic, *Chem. Eng. J.*, 2019, **370**, 136–147.
- 45 Y. Wang, C. Wu, Z. Wu, G. Cui, F. Xie, X. Guo and X. Sun, *Chem. Commun.*, 2018, **54**, 9341–9344.
- 46 L. Yu, X. Peng, F. Ni, J. Li, D. Wang and Z. Luan, *J. Hazard. Mater.*, 2013, **246**, 10–17.
- 47 X. Luo, C. Wang, S. Luo, R. Dong, X. Tu and G. Zeng, *Chem. Eng. J.*, 2012, **187**, 45–52.
- 48 E. S. Dragan and D. F. A. Loghin, *Chem. Eng. J.*, 2013, **234**, 211–222.
- 49 S. Yao, Y. Jia and S. Zhao, *Environ. Technol.*, 2012, **33**, 983–988.
- 50 M. J. López-Muñoz, A. Revilla and G. Alcalde, *Catal. Today*, 2015, **240**, 138–145.
- 51 M. Nishikawa, Y. Mitani and Y. Nosaka, *J. Phys. Chem. C*, 2012, **28**, 14900–14907.
- 52 M. Zhang, R. Sun, Y. Li, Q. Shi, L. Xie, J. Chen, X. Xu, H. Shi and W. Zhao, *J. Phys. Chem. C*, 2016, **120**, 10746–10756.
- 53 P. Kar, T. K. Maji, P. K. Sarkar, P. Lemmers and S. K. Pal, *J. Mater. Chem. A*, 2018, **6**, 3674–3683.
- 54 N. Singh, J. Prakash and R. K. Gupta, *Mol. Syst. Des. Eng.*, 2017, **2**, 422–439.
- 55 A. Tyagi, K. M. Tripathi, N. Singh, S. Choudhary and R. K. Gupta, *RSC Adv.*, 2016, **6**, 72423–72432.
- 56 M. E. Pena, G. P. Korfiatis, M. Patel, L. Lippincott and X. Meng, *Water Res.*, 2005, **39**, 2327–2337.

